Performance of 3DOSEM and MAP algorithms for reconstructing low count SPECT acquisitions

Willem Grootjans[a,c,*], **Antoi P.W. Meeuwis**[a], **Cornelis H. Slump**[b], **Lioe-Fee de Geus-Oei**[a,b,c], **Martin Gotthardt**[a], **Eric P. Visser**[a]

[a] Department of Radiology and Nuclear Medicine, Radboud university medical center, Nijmegen, The Netherlands
[b] MIRA Institute for Biomedical Technology and Technical Medicine, University of Twente, Enschede, The Netherlands
[c] Department of Radiology, Leiden University Medical Center, Leiden, The Netherlands

Received 21 July 2015; accepted 7 December 2015

Abstract

Purpose: *Low count single photon emission computed tomography (SPECT) is becoming more important in view of whole body SPECT and reduction of radiation dose. In this study, we investigated the performance of several 3D ordered subset expectation maximization (3DOSEM) and maximum a posteriori (MAP) algorithms for reconstructing low count SPECT images.*

Materials and Methods: *Phantom experiments were conducted using the National Electrical Manufacturers Association (NEMA) NU2 image quality (IQ) phantom. The background compartment of the phantom was filled with varying concentrations of pertechnetate and indiumchloride, simulating various clinical imaging conditions. Images were acquired using a hybrid SPECT/CT scanner and reconstructed with 3DOSEM and MAP reconstruction algorithms implemented in Siemens Syngo MI.SPECT (Flash3D) and Hermes Hybrid Recon Oncology (Hyrid Recon 3DOSEM and MAP). Image analysis was performed by calculating the contrast recovery coefficient (CRC),percentage background variability (N%), and contrast-to-noise ratio (CNR), defined as the ratio between CRC and N%. Furthermore, image distortion is characterized by calculating the aspect ratio (AR) of ellipses fitted to the hot spheres. Additionally, the performance of these algorithms to reconstruct clinical images was investigated.*

Results: *Images reconstructed with 3DOSEM algorithms demonstrated superior image quality in terms of contrast*

Vergleich der 3DOSEM- und MAP-Algorithmen bei der Rekonstruktion von SPECT-Bildern mit niedriger Zählstatistik

Zusammenfassung

Ziel: *Eine adäquate Rekonstruktion von Single-Photon-Emission-Computed-Tomography(SPECT)-Bildern mit geringer Zählstatistik wird zunehmend wichtiger, insbesondere in Hinsicht auf die Ganzkörper-SPECT und eine Reduktion der Strahlendosis. In dieser Studie wurde die Leistung von verschiedenen Algorithmen bei der Rekonstruktion von Tomographien mit geringer Zählstatistik verglichen.*

Material und Methoden: *Phantom-Experimente wurden mit dem National-Electrical-Manufacturers-Association(NEMA)-NU2-Bildqualitäts(IQ)-Phantom ausgeführt. Verschiedene klinische Situationen wurden durch Füllen des Hintergrunds des Phantoms mit variierenden Konzentrationen von Technetium-Pertechnetat und Indiumchlorid simuliert. Tomographien wurden mit einem SPECT/CT-Scanner acquiriert und mit verschiedenen Algorithmen (ordered subset expectation maximization (OSEM), maximum a posteriori (MAP) und gefilterte Rückprojektion) rekonstruiert. Die für die 3DOSEM-Rekonstruktion verwendeten Algorithmen waren Flash3D (implementiert in Siemens Syngo MI.SPECT) und Hybrid Recon 3DOSEM (implementiert in Hermes Hybrid*

*Corresponding author: W. Grootjans M.Sc., Department of Radiology, Leiden University Medical Center, P.O. Box 9600, 2300 RC Leiden, The Netherlands.
E-mail: W.Grootjans@lumc.nl (W. Grootjans).

and resolution recovery when compared to images reconstructed with filtered-back-projection (FBP), OSEM and 2DOSEM. However, occurrence of correlated noise patterns and image distortions significantly deteriorated the quality of 3DOSEM reconstructed images. The mean AR for the 37, 28, 22, and 17 mm spheres was 1.3, 1.3, 1.6, and 1.7 respectively. The mean N% increase in high and low count Flash3D and Hybrid Recon 3DOSEM from 5.9% and 4.0% to 11.1% and 9.0%, respectively. Similarly, the mean CNR decreased in high and low count Flash3D and Hybrid Recon 3DOSEM from 8.7 and 8.8 to 3.6 and 4.2, respectively. Regularization with smoothing priors could suppress these noise patterns at the cost of reduced image contrast. The mean N% was 6.4% and 6.8% for low count QSP and MRP MAP reconstructed images. Alternatively, regularization with an anatomical Bowhser prior resulted in sharp images with high contrast, limited image distortion, and low N% of 8.3% in low count images, although some image artifacts did occur. Analysis of clinical images suggested that the same effects occur in clinical imaging.

Conclusion: *Image quality of low count SPECT acquisitions reconstructed with modern 3DOSEM algorithms is deteriorated by the occurrence of correlated noise patterns and image distortions. The artifacts observed in the phantom experiments can also occur in clinical imaging.*

Keywords: SPECT, low count image reconstruction, image quality, 3DOSEM, MAP

Recon Oncology). Die Bildqualität wurde durch Berechnung der Kontrastwiederherstellungskoeffizienten (CRC), der Prozent-Hintergundvariabilität (N%) und der Kontrast-Rausch-Verhältnisse (CNR), definiert als das Verhältnis der CRC und N%, quantifiziert. Elliptische Verzerrungen wurden durch die Berechnung der Achsenverhältnisse (AR) ermittelt. Darüber hinaus wurden die verschiedenen Algorithmen anhand der resultierenden Bildqualität von klinischen SPECT-Studien miteinander verglichen.

Ergebnisse: *Bilder, die mit 3DOSEM-Algorithmen rekonstruiert wurden, zeigten eine überlegene Bildqualität in Bezug auf Kontrast und Auflösung im Vergleich zu Bildern, die mit gefilterter Rückprojektion, OSEM und 2DOSEM rekonstruiert wurden. Allerdings treten korrelierte Rauschmuster und Bildverzerrungen auf, welche die Qualität der mit 3DOSEM rekonstruierten Bilder verschlechtert. Die Mittelwerte der AR für die 37-28-22- und 17-mm Kugeln waren 1.3, 1.3, 1.6, und 1.7. Die Hintergrundvariabilität in Flash3D und Hybrid-Recon-3DOSEM-Bildern mit hoher und geringer Zählstatistik stieg von 5.9% und 4.0% auf 11.1% und 9.0%. Der Mittelwert der CNR in Flash3D- und Hybrid-Recon-3DOSEM-Bildern mit hoher und niedriger Zählstatistik verminderte sich von 8.7 und 8.8 auf 3.6 und 4.2. Regularisierung mit smoothing priors können diese Rauschmuster auf Kosten eines reduzierten Bildkontrasts unterdrücken. Wenn die Regularisierung mit einer anatomischen Bowsher prior ausgeführt wurde, ergaben sich scharfe Bilder mit hohem Kontrast, begrenzten Bildverzerrungen und geringer Hintergrund-Variabilität von 8.3%, jedoch können in diesen Bildern Artefakte auftreten. Eine Analyse von klinischen SPECT-Aufnahmen zeigten die gleichen Bildartefakte.*

Schlussfolgerung: *Die Bildqualität der SPECT-Bilder mit niedriger Zählstatistik, welche mit modernen 3DOSEM-Algorithmen rekonstruiert werden, wird durch das Auftreten von korrelierten Rauschmustern und Bildverzerrungen verschlechtert. Die bei den Phantomaufnahmen beobachteten Bildartefakte treten auch bei klinischen SPECT-Bildern auf.*

Schlüsselwörter: SPECT, Bildrekonstruktion mit niedriger Zählstatistik, Bildqualität, 3DOSEM, MAP

Introduction

Imaging with γ-emitting radionuclides is important for the detection and staging of a variety of diseases. Single photon emission computed tomography (SPECT) is a well-established tomographic imaging technique for which a large variety of radiotracers is available, offering the possibility to reconstruct a three dimensional source distribution of a γ-emitter within the patient. Over the last decades, there have been considerable advancements in image reconstruction for SPECT with the development of a variety of iterative reconstruction schemes incorporating correctional techniques to model system response, photon scattering and attenuation [1–3]. The most widely used iterative reconstruction

algorithms in today's clinical practice are the ordered subset expectation maximization (OSEM) schemes, as proposed by Hudson and Larkin [4]. The key component in these algorithms is the implementation of a maximum likelihood expectation maximization (MLEM), described by Shepp and Vardi [5], which updates an estimated image during each iteration according to a log-likelihood merit function. The OSEM algorithms are essentially a fast implementation of the MLEM scheme, which divides the acquired projection data in subsets to reduce computational burden [4].

Although the MLEM allows the modeling of various effects, such as photon scatter, photon attenuation, and system response, the amount of image noise tends to increase for increasing numbers of iterations, particularly in low count acquisitions. However, early termination of image reconstruction at a few iterations is undesirable since an acceptable convergence for all points in the image is not guaranteed [6]. Constraining noise propagation during image reconstruction can be performed through incorporation of prior assumptions about the underlying radioactivity distribution into image reconstruction, which can stabilize image convergence by preventing unacceptable enhancement of image noise [6]. Such regularization step during image reconstruction can be performed using a Bayesian framework, which is referred to as maximum a posteriori (MAP) estimations [7–9].

These developments have resulted in significant improvements in image quality in terms of contrast, noise reduction, resolution, and improved image quantification enabling reconstruction of SPECT images with lower count statistics [10–14]. This is particularly interesting in the view of reduction of acquisition time for the purpose of whole body SPECT imaging, optimizing clinical work-flow and increasing patient throughput, or facilitation of radiation dose reduction [15–17].

The purpose of this study was to investigate the performance of several state-of-the-art ordered subset expectation maximization algorithms using 3D geometric modeling of system response (3DOSEM) for reconstructing low count acquisitions under clinically realistic imaging conditions. Furthermore, several MAP reconstruction algorithms were evaluated. To this end, image quality of standardized phantom experiments and clinical images was assessed.

Materials and Methods

NEMA NU2 Image Quality Phantom Experiments

Phantom experiments were conducted using the National Electrical Manufacturers Association (NEMA) NU2 image quality (IQ) phantom [18]. The body of the IQ phantom consists of a polymethylmethacrylate (PMMA) casing which contains six fillable spheres together with a lung insert. The background compartment of the phantom was filled with an aqueous solution containing 69.3 MBq of pertechnetate ($^{99m}TcO_4^-$), resulting in an activity concentration of 7.14 kBq·mL^{-1}. This activity concentration corresponds to a total injected activity of 500 MBq of a technetium conjugated compound into a patient of 70 kg. During these experiments, the activity concentration in the spheres was four times higher, resulting in a background to sphere contrast ratio of 1:4. To simulate biological clearance and physical decay in the human body, phantom acquisitions were performed at multiple time points, simulating 100%, 50% and 14% whole body retention of a ^{99m}Tc conjugated compound. Experiments with indium were performed by filling the background compartment with 25.6 MBq of indiumchloride ($^{111}InCl_3$), resulting in an activity concentration of 2.64 kBq kBq·mL^{-1} corresponding to a total injected activity of 185 MBq of an indium conjugated compound into a patient of 70 kg.

Image Acquisition

SPECT/CT images were obtained with a Symbia Truepoint T16 SPECT/CT scanner (Siemens Medical Systems, Hoffman Estates, IL, USA). The ^{99m}Tc SPECT images were acquired using a low energy high resolution (LEHR) collimator with a fixed circular orbit with a radius of rotation of 30 cm, 128 views (64 views per camera head) in step-and-shoot mode and a 360° rotation range. The ^{111}In SPECT images were obtained using similar acquisition setting with a medium energy low penetration (MELP) collimator. The recording time per view was varied for different acquisitions and was set to 9 and 45 seconds for ^{99m}Tc acquisitions, and to 9, 15, and 45 seconds for ^{111}In acquisitions. The SPECT images acquired with a duration of 45 seconds per view correspond to the standard acquisition protocol at this institution. The rationale for a view duration of 15 seconds and 9 seconds was to investigate the possibility to perform either multiple bed position SPECT (3 bed positions) and whole body SPECT (five bed positions). The view durations were chosen so that the entire patient examination would not exceed that of the current clinical SPECT protocol. Subsequently, after the SPECT acquisition, a low dose (LD) CT scan with a reference X-ray tube current time product and peak voltage of respectively 125 mAs and 130 kVp, respectively, was acquired for the purpose of attenuation correction and evaluation of co-registration. Modulation of X-ray tube current was performed using CARE Dose4D [19].

Patient cases

In addition to analysis of phantom acquisitions, image quality of clinical SPECT images, reconstructed with different reconstruction algorithms, was investigated. To this end, typical low count nuclear medicine examinations with technetium and indium were investigated, including parathyroid and somatostatin receptor SPECT/CT. Using information from other imaging modalities such as contrast enhanced diagnostic CT and ultrasound (US) images, SPECT images were evaluated for the occurrence of artefacts.

Image Reconstruction

Filtered back projection and ordered subset expectation maximization

The SPECT images were reconstructed with different reconstruction settings and algorithms using the Siemens Syngo MI.SPECT application (E.soft 2009a, 8.1.15.7 service pack 2, Siemens AG, Berlin and München, Germany) and the Hermes HybridRecon oncology package (Hermes Medical Solutions, Stockholm, Sweden). SPECT images were reconstructed with filtered-back-projection (FBP) and iterative OSEM algorithms. Both OSEM algorithms without and with geometric point spread function (PSF) modeling (using both fan beam (2D) and cone beam (3D)), were used. The image update in the OSEM scheme can be considered as successive forward and back-projection operations and can be mathematically described using equation (1) [4]

$$\bar{f}_i^{(k+1)} = \frac{\bar{f}_i^{(k)}}{\sum_{j \in S_n} M_{i,j}} \sum_{j \in S_n} M_{i,j} \frac{g_j}{\left(\Sigma_{i'} M_{i',j} \bar{f}_{i'}^{(k)}\right)} \tag{1}$$

Here, $\bar{f}_i^{(k)}$ and $\bar{f}_i^{(k+1)}$ are the old and new estimate of the i^{th} (the index' in the back-projection term indicates that this term is calculated first) voxel at the k^{th} iteration, g_j is the measured projection value at projection bin j, $M_{i,j}$ is the system matrix describing the probability that a photon emitted from voxel i is captured at projection bin j, and S_n is the n^{th} subset. The term $\frac{g_j}{\left(\Sigma_{i'} M_{i',j} \bar{f}_{i'}^{(k)}\right)}$, describes the ratio between the measured g_j and the forward projected (estimated) projection value $\Sigma_{i'} M_{i,j} \bar{f}_{i'}^{(k)}$. After the iteration is completed, the image elements are updated to the new estimate and the algorithm starts with the next iteration. Images were reconstructed with an axial matrix size of 128 × 128 voxels (resulting in an isotropic voxel size of 4.8 mm) and standard post reconstruction filtering was performed on the OSEM-reconstructed images with a 3D Gaussian filter kernel with a FWHM of 2.0 times the pixel spacing (9.6 mm).

Maximum a posteriori reconstructions

In addition to the 3DOSEM reconstructions (Siemens Flash3D and Hermes Hybrid Recon 3DOSEM), several MAP reconstruction schemes were evaluated. The MAP reconstruction is generated by adding a regularizing prior to the 3DOSEM reconstruction in the Hermes Hybrid Recon Oncology software. Implementation of this regularization step into the iterative image reconstruction scheme of Hermes Hybrid Recon Oncology is accomplished by using the one-step-late (OSL) approach, as described by Green and colleagues [7,8]. The mathematical formulation of the OSL algorithm is provided by equation (2).

$$\bar{f}_i^{(k+1)} = \frac{\bar{f}_i^{(k)}}{\sum_{j \in S_n} M_{i,j} + \beta \frac{\partial}{\partial \bar{f}_i^{(k)}} U\left(\bar{f}_i^{(k)}\right)} \times \sum_{j \in S_n} M_{i,j} \frac{g_j}{\left(\Sigma_{i'} M_{i',j} \bar{f}_{i'}^{(k)}\right)} \tag{2}$$

Here, $\beta \frac{\partial}{\partial \bar{f}_i^{(k)}} U\left(\bar{f}_i^{(k)}\right)$ is the Bayesian prior and is represented as a derivative of an energy function U and weighing factor β in the update term. During this regularization step, voxels which do not meet the specific criteria described by the energy function within the prior will be penalized during image reconstruction. The result is that the voxel intensity is forced to have either a lower or higher intensity.

Available priors for the MAP reconstruction include those with a quadratic smoothing prior (QSP), a median root prior (MRP) and an X-ray CT based anatomical prior, also known as a Bowsher prior [8]. Image reconstruction with a QSP attempts to smooth the image, including the boundaries between different structures, permitting only gradual changes in voxel intensity. When the estimated average intensity of neighboring pixels of image element approximates that of the image element itself, the neighborhood is considered to be smooth and the update process is the same as during OSEM reconstruction. However, if the value of the image element is higher than the neighboring elements, the new estimate of the element is forced to be lower. Conversely, when the value of the image element is lower, the value of new estimate is forced to be higher. The QSP prior is provided by equation (3).

$$\frac{\partial}{\partial \bar{f}_i^{(k)}} U\left(\bar{f}_i^{(k)}\right) = \sum_{b \in N_i} w_{ib} \left(\bar{f}_i^{(k)} - \bar{f}_b^{(k)}\right) \tag{3}$$

Here N_i is a set of voxels that are in the neighborhood of voxel i, w_{ib} is the prior weight which is defined as the inverse of the distance of the neighboring voxel b from the center of voxel i, $\bar{f}_i^{(k)}$ and $\bar{f}_b^{(k)}$ are the values of voxel i and neighbor b respectively for the k^{th} estimate. The MRP is essentially a slight modification of the QSP, attempting to preserve edges during image reconstruction. In contrast to comparing the value of the central image element to the mean value of the neighboring image elements as implemented in the QSP, the MRP compares the value of the central image element to the median value of the neighboring image elements. For both the QSP and MRP, the neighborhood size is set to 3×3×3 voxels.

The derivative of the energy function of the anatomical Bowsher prior is similar to the quadratic smoothing prior, with the exception that the selected voxels constituting the neighborhood is determined according to a similarity criterion based on CT image intensities. This similarity criterion finds the most similar voxels by comparing the absolute difference

in Hounsfield units (HU) between the center and neighboring voxels on the CT images.

The strength of the regularization step during MAP image reconstruction is controlled by the value for the Bayesian weight (β). During this study, the value for β is fixed and set to 0.3 (as recommended by the manufacturer). No post reconstruction filtering was performed on the images reconstructed with the MAP algorithms. Attenuation correction was performed on the OSEM and MAP reconstructions using a CT derived μ-map. Reconstructions were performed with a varying number of iterations and subsets in order to determine optimal reconstruction settings for different acquisitions.

Analysis of Image Quality

Analysis of image quality is performed by calculating the percentage contrast (designated the contrast recovery coefficient (CRC) here) of the visible spheres, and the percentage background variability, as defined in the NEMA-NU2 2012 guidelines [18]. Sphere visibility was defined when the average number of counts in the sphere ROI exceeded that of the average number of counts in the background plus the standard deviation of the background. The CRC of sphere j was calculated using equation (4).

$$CRC_j = \frac{\left(\frac{c_j}{c_b} - 1\right)}{\left(\frac{a_j}{a_b} - 1\right)} \cdot 100\% \quad (4)$$

Here, c_j is the mean number of counts in a circular region of interest (ROI) matched to the inner diameter of sphere j that is being measured, c_b is the mean number of counts in 60 background ROIs placed within 5 image slices (12 ROIs in the central slice and 12 ROIs in the slices at ±1 cm and ±2 cm from the central slice), with a diameter equal to that of the sphere ROI j. The percentage background variability was calculated for each sphere using equation (5).

$$N_j = \frac{SD_j}{c_{b,j}} \cdot 100\% \quad (5)$$

Where SD_j is the standard deviation between all of the background ROIs and $c_{b,j}$ is the mean of the background ROIs. For calculation of the CRC of the spheres, a ROI mask was placed in the central axial image. The image quality parameters were calculated using Matlab scripts (Mathworks Matlab 2012a, Natick, Massachusetts, U.S.A) developed for this purpose.

In order to objectively compare the performance of different reconstruction algorithms, the contrast-to-noise ratio (CNR) was calculated for the different spheres. The CNR, which is not a standard NEMA parameter, was defined as the quotient of the CRC and the corresponding percentage background variability of that sphere. The optimal number of iterations for each acquisition was defined when further increasing the number of iterations resulted in an increase in CNR of less than 5% for the smallest sphere.

In addition to contrast and noise, specific image distortions were observed in 3DOSEM reconstructed SPECT images. In particular, elliptical distortions have been reported of spherical objects [20]. In this regard, quantification of these image distortions was performed by determining the aspect ratios (ARs) of the ellipses, as described in [20]. After background subtraction, an ellipsoid was fitted through calculation of second moments of the segmented spheres using the ImageJ processing package Fiji [21]. The AR was then calculated by determining the ratio of the major and minor axis of the fitted ellipses.

Results

3D ordered subset expectation maximization (OSEM)

In general, images reconstructed with the 3DOSEM algorithms (Flash3D and Hybrid Recon 3DOSEM) exhibited improved contrast of the hot spheres and smaller amounts of image noise, as compared to the FBP, OSEM, and 2DOSEM reconstructions. Analysis of sphere visibility revealed that the 10 mm and 13 mm spheres were not visible in any of the 3DOSEM reconstructed images. Although the shape of larger structures (e.g. the 37 mm diameter sphere and lung insert) of the phantom were adequately depicted in the high count images, smaller structures (i.e. the 28 mm, 22 mm, and 17 mm spheres) appeared to be distorted in an elliptical fashion. Fig. 1 depicts the 3DOSEM reconstructed images of the NEMA phantom with different activity concentrations.

The shape of the spheres and lung insert became increasingly more distorted with decreasing activity concentrations and shorter image acquisition times. Evaluation of co-registration with CT images revealed that spatial matching of SPECT and CT images is decreased due to these image distortions. Furthermore, in low count acquisitions, the distortions appeared more irregular star-shaped due to confluence of the spheres with the noisy background.

In addition to the shape distortions of different structures within the phantom, a decreasing number of spheres were visible in low count acquisitions. Sphere visibility and overall appearance was not considerably different between images reconstructed with Flash3D and Hybrid Recon 3DOSEM. Similar results were obtained with ^{111}In, with decreased sphere visibility and more prominent imaging distortions in low count imaging. Table 1 summarizes the ARs of the spheres in Flash3D and Hybrid Recon 3DOSEM reconstructed images.

Background variability and image contrast

Image quality in 3DOSEM reconstructed images was severely degraded by the occurrence of irregular noise patterns in the background compartment of the phantom. These

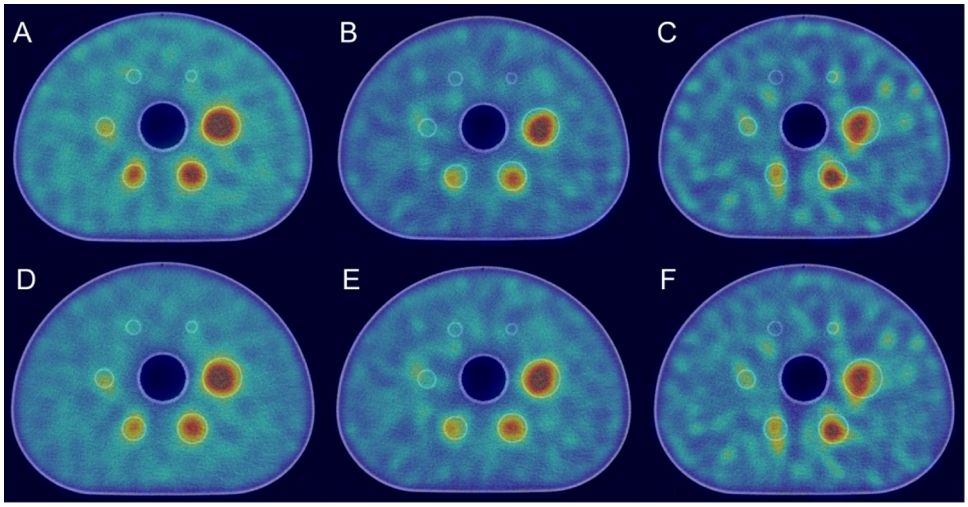

Figure 1. Images obtained with different activity concentrations of pertechnetate ($^{99m}TcO_4^-$) in the background, reconstructed with Flash3D and Hybrid Recon 3DOSEM. The Flash3D images (A-C) are reconstructed with 10 iterations and 16 subsets, whilst the Hybrid Recon 3DOSEM images (D-F) are reconstructed with 6 iterations and 16 subsets. The first column depicts images acquired with an activity concentration of 7.1 kBq ml^{-1}, the second column with 3.6 kBq ml^{-1}, and the third column with 1.0 kBq ml^{-1}.

Table 1
Aspect ratios (ARs) of the spheres of the National Electrical Manufacturers Association (NEMA) phantom in the Flash3D and Hybrid Recon 3D ordered subset expectation (3DOSEM) reconstructed images for different image acquisition times and background activity concentrations of pertechnetate ($^{99m}TcO_4^-$). When the sphere was not visible in the image, this is indicated by an'x'.

	Flash3D						Hybrid Recon 3DOSEM					
	7.1 kBq/ml		3.6 kBq/ml		1.0 kBq/ml		7.1 kBq/ml		3.6 kBq/ml		1.0 kBq/ml	
Sphere diameter [mm]	45 s	9 s	45 s	9 s	45 s	9 s	45 s	9 s	45 s	9 s	45 s	9 s
37	1.04	1.58	2.24	1.25	1.33	1.35	1.04	1.25	1.03	1.44	1.21	1.27
28	1.27	1.19	1.05	1.79	1.29	1.64	1.25	1.27	1.10	1.18	1.16	1.64
22	1.44	1.38	1.06	1.26	2.41	x	1.51	1.26	1.12	2.36	2.40	x
17	1.57	1.94	1.15	x	1.76	x	1.53	1.34	1.68	x	2.05	x
13	x	x	x	x	x	x	x	x	x	x	x	x
10	x	x	x	x	x	x	x	x	x	x	x	x

Table 2
Optimal number of iterations for Flash3D and Hybrid Recon 3D ordered subset expectation maximization (3DOSEM) reconstructed images under different imaging conditions using 99m-technetium pertechnetate ($^{99m}TcO_4^-$) and 111-indium chloride ($^{111}InCl_3$) together with the mean count density of the projections.

Activity Concentration [kB/ml]	Radionuclide	Count density projection (counts·cm^{-2})	Recording time per view [s]	Optimal Number of Iterations Flash3D	Optimal Number of Iterations Hybrid Recon 3DOSEM
7.1	^{99m}Tc	46 ± 3.1	45	14	6
7.1	^{99m}Tc	11 ± 0.67	9	6	4
3.6	^{99m}Tc	31 ± 2.0	45	10	5
3.6	^{99m}Tc	6.3 ± 0.39	9	6	4
1.0	^{99m}Tc	25 ± 1.7	45	10	5
1.0	^{99m}Tc	5.8 ± 0.34	9	2	2
2.6	^{111}In	46 ± 36	45	10	6
2.6	^{111}In	16 ± 12	15	10	6
2.6	^{111}In	2.5 ± 1.9	9	6	4

Data are represented as mean ± standard deviation.

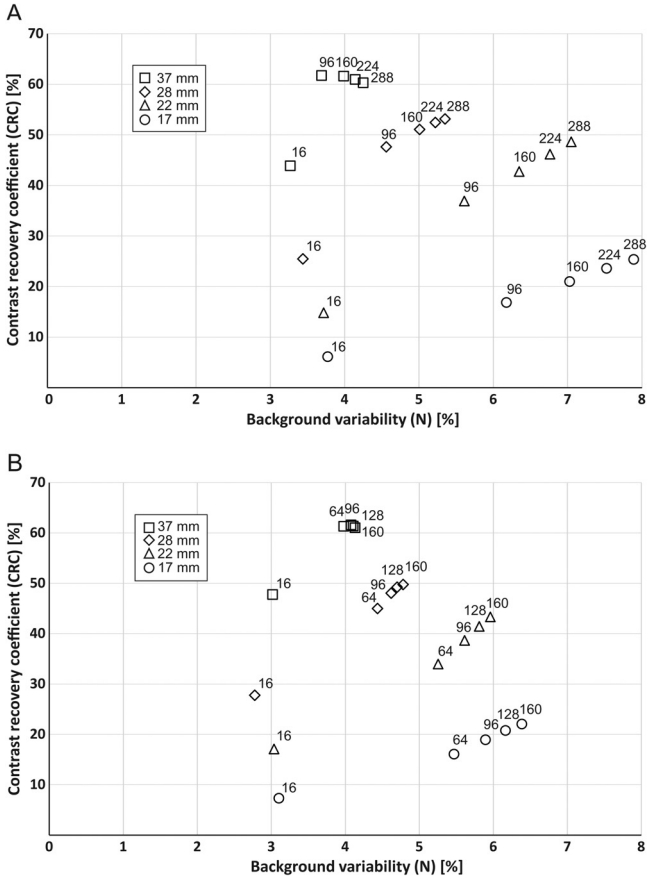

Figure 2. Change in contrast recovery coefficient (CRC) and background variability for different sphere diameters as a function of the number of updates (obtained through multiplication of the number of iterations and subsets) in Flash3D and Hybrid Recon 3DOSEM reconstructed images. The number of subsets during image reconstruction was 16. Images were acquired with an activity concentration of 7.1 kBq ml^{-1} of pertechnetate ($^{99m}TcO_4^-$) in the background compartment and an acquisition time of 45 seconds per view. A) Change in CRC and background variability for Flash3D images, B) Change in CRCand background variability for Hybrid Recon 3DOSEM reconstructed images.

patterns typically consisted of clusters of voxels with a high intensity that were more or less equally distributed throughout the entire background compartment.

In general, the CRCs of the spheres in the Flash3D reconstructed images were higher when compared to the Hybrid Recon 3DOSEM reconstructed images. However, the background variability was also increased in these images. Image reconstruction with more iterations increased the CRC of the smaller spheres, at the cost of an increased background variability. This is shown in Fig. 2, depicting the CRC of the spheres as a function of the numbers of updates, defined as the product of the number of iterations and subsets, for Flash3D and Hybrid Recon 3DOSEM images.

Furthermore, the number of iterations yielding an optimal CNR is decreased in low count acquisitions when compared to the high count acquisitions due to the sharp increase in background noise. The optimal number of iterations for different SPECT acquisitions reconstructed with the 3DOSEM algorithms are summarized in Table 2. There were no relevant differences in the value of the CNRs of Hybrid Recon 3DOSEM and Flash3D reconstructed images. The CNR of the spheres as a function of background variability for Hybrid Recon 3DOSEM and Flash3D images for different SPECT acquisitions with $^{99m}TcO_4^-$ are depicted in Fig. 3.

Maximum a posteriori (MAP) reconstructions

Regularization using a QSP or MRP resulted in suppression of noise at the cost of reduced image contrast and edge preservation. This blurred appearance was not observed when the anatomical Bowsher prior was used. Images reconstructed with the anatomical Bowsher prior were characterized by improved edge preservation, with a sharp fall-off in intensity between the transition of different structures, and the absence of shape distortions in the images. However, the walls of different spheres became enhanced in a number of these images, producing ring-like artifacts. This is demonstrated in Fig. 4, depicting MAP images reconstructed with the three different priors. The CNR values as a function of background variability of the MAP reconstructed images with different background activity concentrations of $^{99m}TcO_4^-$ and image acquisition times are depicted in Fig. 3.

Clinical Imaging

Since the observed image artifacts occurred in phantom experiments using activity concentrations that resembled clinical imaging conditions, clinical low count images were evaluated for evidence of these, or similar, artifacts. In clinical practice, nuclear medicine examinations in which low count imaging conditions typically occur are parathyroid and somatostatin receptor SPECT imaging. The first clinical case concerns a 65 year old male patient who presented with hypercalcemia due to primary hyperparathyroidism and was referred to our department for parathyroid SPECT imaging with technetium labeled sestamibi. Fig. 5 depicts the ultrasound (US), low dose (LD) CT and 3DOSEM and MAP reconstructed SPECT/CT images of this patient. The SPECT images revealed asymmetrical increased uptake at the right caudal lobe of the thyroid. In addition, US imaging showed a spherical lesion suspicious for a parathyroid adenoma. Histopathological evaluation after surgical extirpation of the lesion confirmed the presence of an oncocytic parathyroid adenoma. Evaluation of the 3DOSEM reconstructed SPECT images revealed that the lesion had a typical elongated appearance that was similar to the shape distortions observed during the phantom experiments. However, the LDCT and US

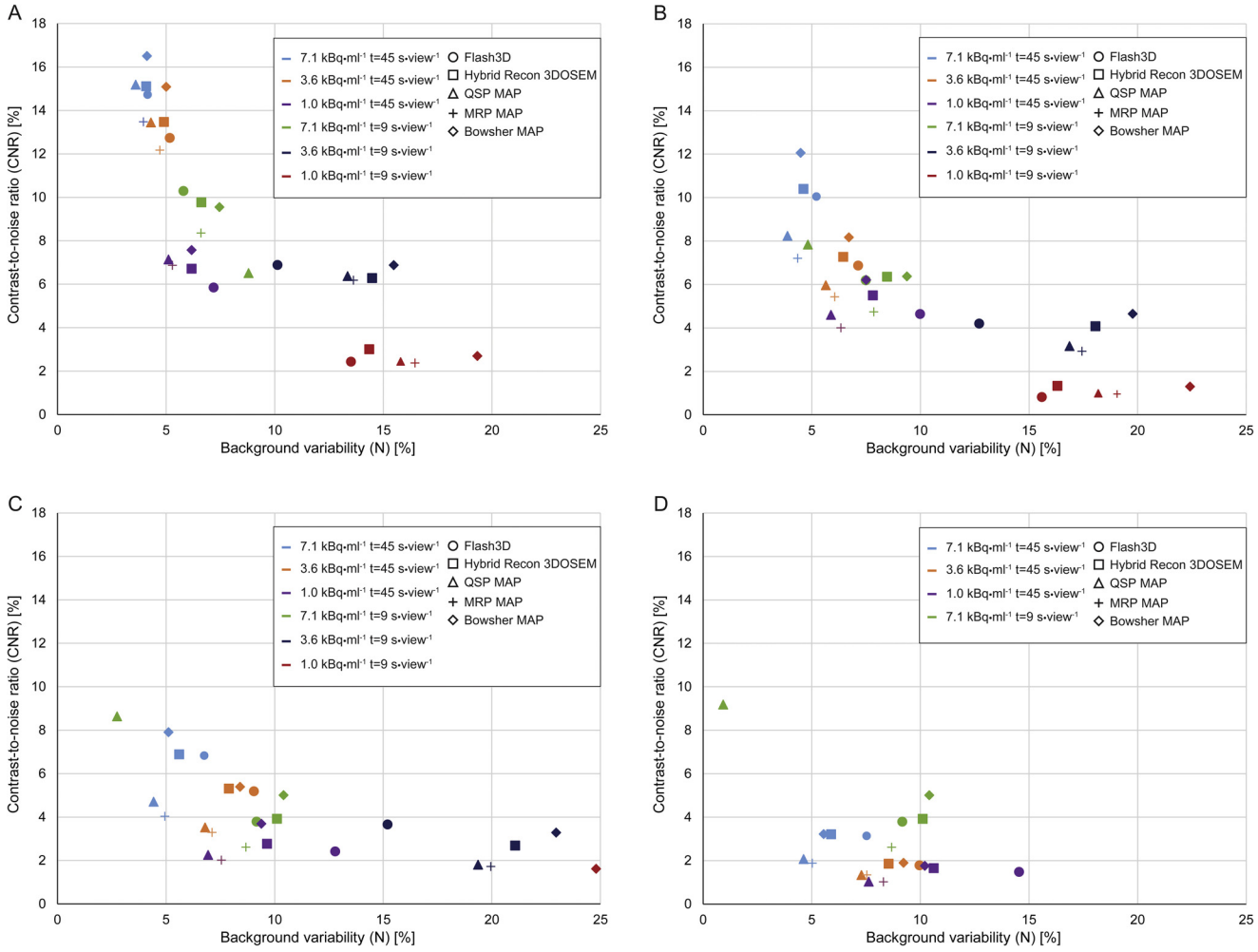

Figure 3. Contrast-to-noise ratio (CNR), defined as the ratio between the contrast recovery coefficient (CRC) and the background variability, of different spheres under varying imaging conditions as a function of background variability. Images were acquired with different activity concentrations of pertechnetate ($^{99m}TcO_4^-$) and image acquisition times. The 3DOSEM images were reconstructed using optimal reconstruction settings, whereas MAP images were reconstructed using a Bayesian weight of 0.3, 4 iterations, and 16 subsets. Obtained CNRs as a function of background variability for different imaging conditions and reconstruction algorithms for A) 37 mm sphere, B) 28 mm sphere, C) 22 mm sphere, D) 17 mm sphere.

images showed a lesion with a more spherical morphology. Reconstruction with the QSP and MRP MAP algorithms showed similar elongated appearance of the lesion, although image contrast was reduced in these images. Image reconstruction with the Bowsher prior resulted in an erratic fragmented appearance of the lesion in the SPECT images, which is an unlikely distribution of the radiotracer within the adenoma.

Fig. 6 depicts the second patient case involving a 67 year old male with known liver metastases of a carcinoid tumor. This patient showed radiographic and clinical signs of progressive disease and imaging with ^{111}In-pentetreotide was performed in order to determine whether this patient was eligible for therapy with radiolabeled somatostatin analogs (such as [^{177}Lu-DOTA0,Tyr3]octreotate or [^{90}Y-DOTA^0,Tyr^3]octreotide). The acquired ^{111}In-pentetreotide SPECT images revealed multiple carcinoid lesions within the liver. However, when the shape and appearance of the lesions in SPECT images are compared to the contrast-enhanced CT images, the appearance of a number of lesions on SPECT appear to be elliptically distorted in contrast to the almost perfectly spherical appearance on CT. The QSP and MRP MAP reconstructions showed decreased background variability and reduced image contrast. Furthermore these images showed similar distortions, as observed in the 3DOSEM images. Image reconstruction with the anatomical Bowsher prior yielded highly erratic images in which lesion visibility was reduced.

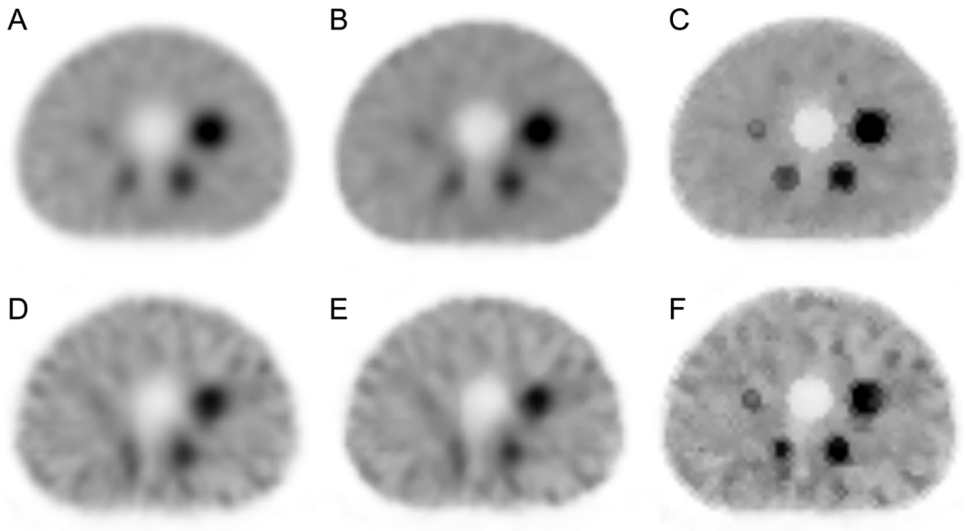

Figure 4. Maximum a posteriori (MAP) reconstructions using a quadratic smoothing prior (QSP) (first column), median root prior (MRP) (second column), and an anatomical 'Bowsher' prior (third column). The images are acquired using an activity concentration of 7.1 kBq ml^{-1} (first row) and 1.0 kBq mL^{-1} (second row) of pertechnetate ($^{99m}TcO_4^-$), with an acquisition time of 45 seconds per view.

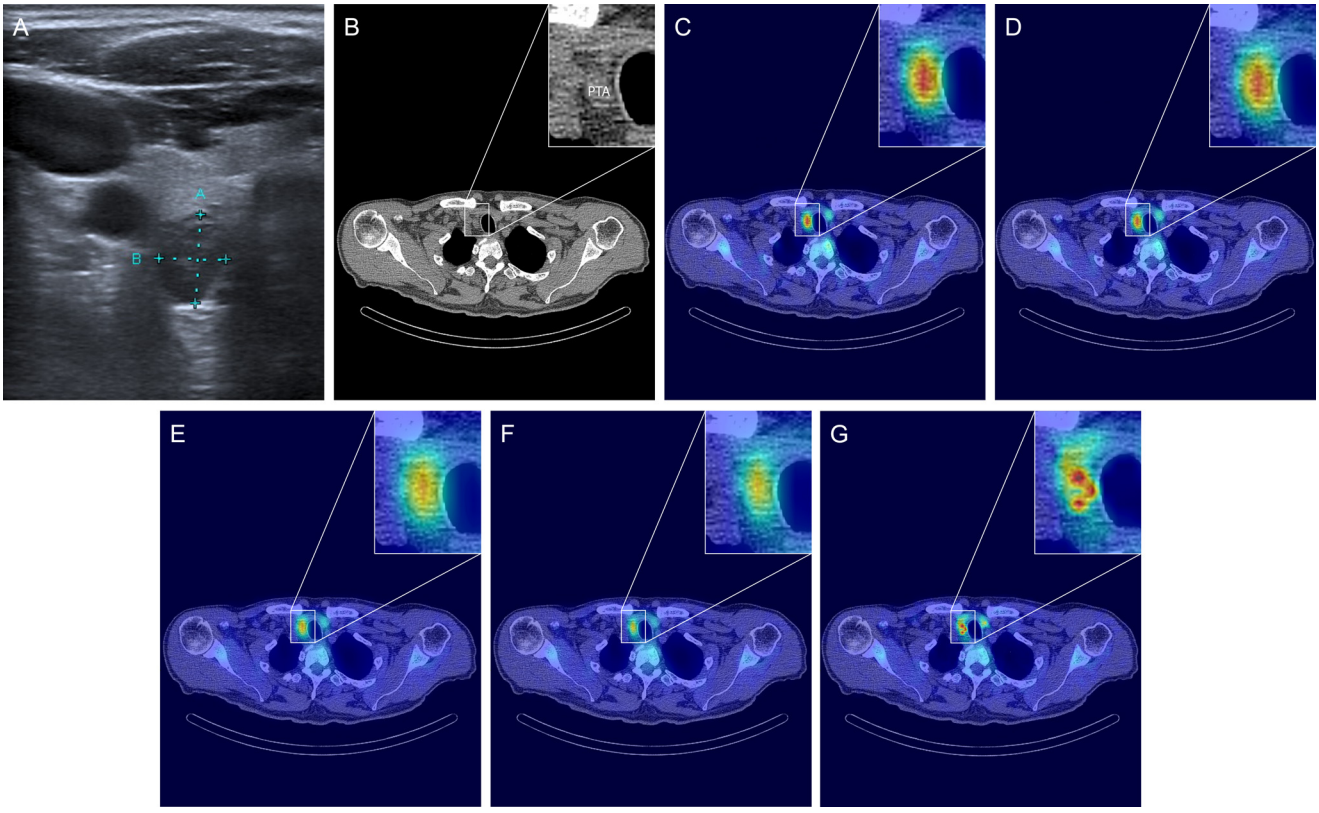

Figure 5. Ultrasound (US) and SPECT/CT images of a patient presenting with primary hyperparathyroidism. A) US images showing a spherical lesion dorsal of the caudal part of the right thyroid lobe, B) low dose (LD) CT imaging demonstrating a lesion with spherical morphology at the site of sestamibi uptake, C) Flash3D reconstructed image fused with LDCT, D) Hybrid Recon reconstructed image fused with LDCT, E) QSP MAP reconstructed image fused with LDCT, F) MRP MAP reconstructed image reconstructed with LDCT, G) Anatomical Bowsher MAP reconstructed image fused with LDCT. PTA = Parathyroid adenoma.

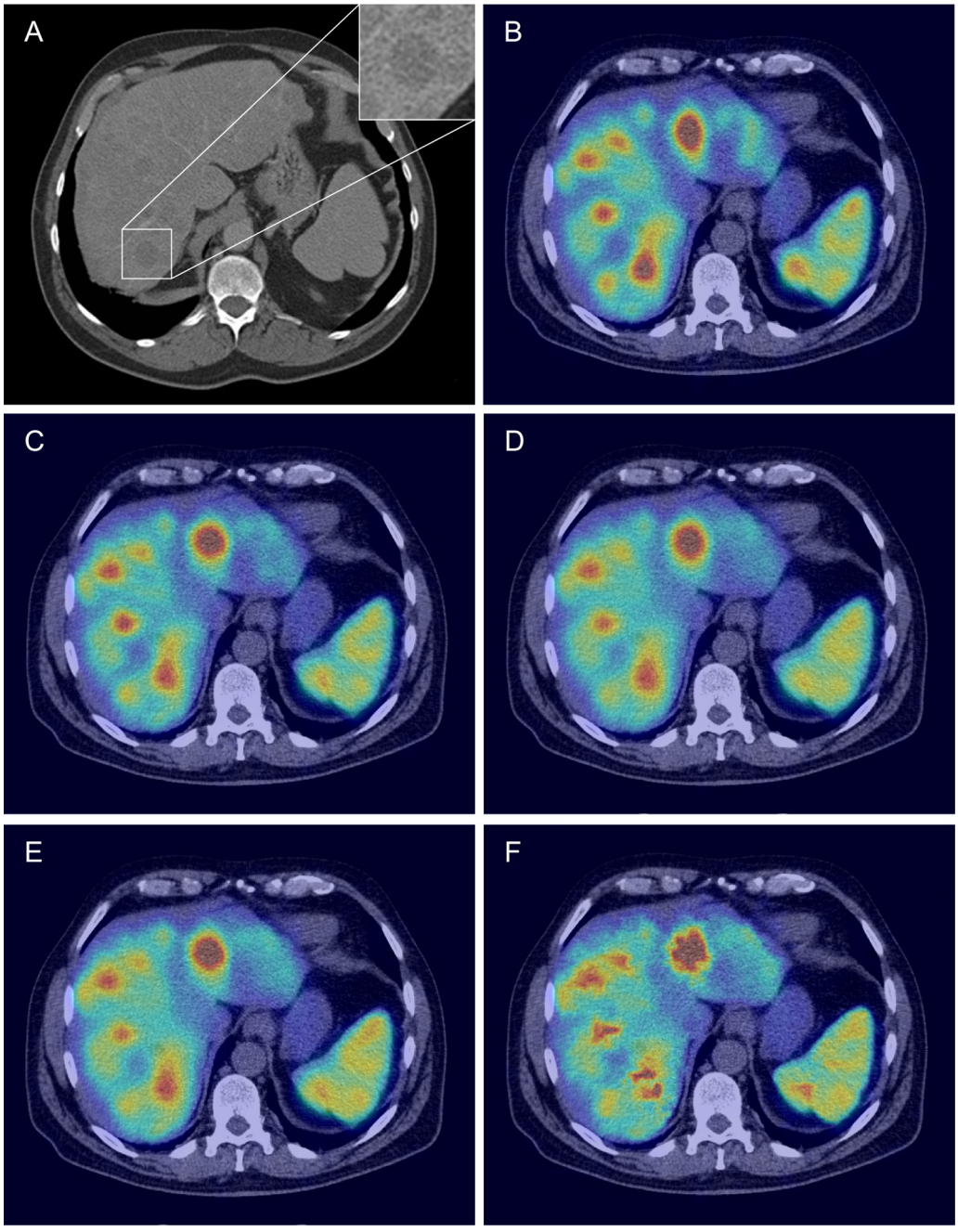

Figure 6. Somatostatin receptor (SR) SPECT performed with ^{111}In-pentreotide and contrast enhanced diagnostic CT (CECT) imaging in a patient 67 year old male patient with multiple metastatic carcinoid lesions in the liver. A) CECT imaging with ioversol (OptiRay 300), B) Flash3D, C) Hybrid Recon 3DOSEM, D) QSP MAP, E) MRP MAP, F) Anatomical Bowsher prior MAP.

Discussion

In this study, the performance of several OSEM and MAP reconstruction algorithms for reconstruction of low count SPECT acquisitions was investigated. In general, the 3DOSEM algorithms demonstrated improved contrast and lower noise levels when compared to FBP, OSEM and 2DOSEM algorithms. However, a major factor which reduces image quality for the 3DOSEM reconstructed images is the occurrence of irregular noisy patterns in the reconstructed images. Particularly problematic is that these noise patterns are spatially correlated, forming clusters which are intensified when count statistics are reduced or when image reconstruction is performed with a high number of iterations. Since the intensity of this spatially correlated noise in the background was similar to that of the

'hot' spheres, these can be mistaken for regions with uptake.

The choice of reconstruction algorithm and type of convolution kernel used in the reconstruction algorithm significantly affect the magnitude and texture of noise [22,23]. In particular, the update mechanism of a typical MLEM implementation contributes to the "evaporation" effect, wherein counts in regions of low activity gravitate towards regions of high activity [24]. The update step in the MLEM reconstruction essentially comprises of a ratio comparing the acquired data with the data model, which appears in a denominator. Constraining the value of this ratio is typically achieved by setting a minimum threshold, thereby preventing a division by zero or very small numbers. Lowering the threshold yields images with more noise whilst increasing the threshold results in amplification of the evaporation effect, enhancing the observed irregular noise patterns. In low count acquisitions, these effects are exaggerated given that some projection elements contain only very few or no counts. In this regard, an interesting approach to reduce these effects is to process the noisy projection data [25,26]. In a study, Vija et al report that pre-processing of SPECT projections with a Pixon-based algorithm is feasible [25]. However, it is also associated with significant pitfalls that in the current state likely outweigh the benefits. In another study, Takalo and colleagues report the use of an adaptive autoregressive model to pre-process SPECT projection data and postfilter reconstructed images to reduce noise in SPECT images [26]. Although such strategies are interesting, further development and validation of these methods using clinical data is required.

The shape distortions in the 3DOSEM reconstructions are, at least partially, attributable to inaccuracies in system response modeling and high noise content in the projections. The effect of PSF modeling on image distortion is emphasized by Römer et al, reporting improved shape fidelity of 3DOSEM compared to 2DOSEM, particularly in the axial direction [27]. In Flash3D and Hybrid Recon 3DOSEM, depth-dependent resolution and system response is modeled by assuming a cone-beam. However, this geometric modeling of the system response is not entirely accurate, given the specific geometry of the collimator holes (which are hexagonal instead of cylindrical) and detector response [24]. Inaccuracies in system modeling result in propagation of systemic errors during image reconstruction [28]. Alternatively, system response can be measured, which is expected to yield more accurate convergence of the images. This approach is used in the successor of Flash3D, designated xSPECT (Siemens Medical Solutions, Knoxville Tennessee, USA), where the actual system response is measured over the entire field of view (FOV) across all relevant imaging distances [24].

The problem of non-linear noise propagation of iterative image reconstruction is well-known and has been described thoroughly in literature [29–31]. In particular, a general unified framework to accurately describe noise propagation during iterative image reconstruction proves to be difficult [28]. Although accurate modeling of noise has a great potential for improving image quality and quantitative accuracy, early termination of image reconstruction at few iterations and characteristics of the algorithms itself hinder accurate prediction of noise propagation [28].

In the present study we evaluated the performance of several regularizing priors implemented in a MAP reconstruction scheme for the purpose of noise suppression. Guidance of image reconstruction using priors resulted in the possibility to reconstruct images with a sufficient number of iterations whilst constraining noise propagation. However, this comes at the cost of image resolution, contrast, and or edge preservation [8]. Image reconstruction algorithms using a MAP estimation have the potential to improve image reconstruction when suitable priors are used. With the advent of hybrid SPECT/CT imaging systems, addition of information obtained from CT images to guide SPECT reconstructions is an interesting concept [32]. These anatomical priors can be based on blurred anatomical labels, mutual information and joint entropy, or on local anatomical information [33,34]. Typically, reconstruction algorithms employing anatomical priors can be classified into edge-based and region based. The edge-based methods use information about the edges of different structures within the image in order to avoid smoothing of the boundaries separating these regions. The region-based methods first create a template image and the difference between the template image and reconstructed image is incorporated into the cost function during image reconstruction.

However, the choice of a suitable prior is difficult and a poor prior choice can result in convergence of the reconstruction towards an undesirable solution. Furthermore, care should be taken when performing image reconstruction using prior assumptions based on other imaging modalities, such as CT or MRI data, since these data sets are fundamentally different from SPECT data. Anatomical information cannot always be directly translated to radiotracer uptake, particularly in the presence of confounding factors such as disease and patient to patient variation. The problems related to such priors are clearly demonstrated in reconstructed phantom images, where generation of ring-like artefacts of the smaller spheres indicated a fundamentally wrong assumption about the underlying radioactivity distribution using the CT data. Furthermore, clinical data reconstructed with the anatomical prior resulted in erratic images that were not suitable for use in a clinical setting.

Conclusion

The results of this study demonstrate the difficulties associated with image reconstruction of low count acquisitions in SPECT and emphasize the importance of the regularization of noise propagation in the images. Particularly in low count acquisitions, the occurrence of shape distortions and increasingly, involvement of the background with erroneous regions of higher uptake, results in severe degradation of image quality. It was demonstrated that the addition of a regularizing

prior improved control of noise propagation, though at the cost of edge preservation and image contrast. Furthermore, there is supporting evidence that the specific artefacts observed can occur during SPECT imaging under clinical imaging conditions. Although these specific artefacts would not have resulted in a direct change in patient management in the presented clinical cases, physicians should be aware that these specific artefacts can occur in clinical imaging.

Acknowledgements

W. Grootjans receives an educational grant from Siemens Healthcare, The Hague, The Netherlands

References

[1] Tsui BMW, Hu HB, Gilland DR, Gullberg GT. Implementation of simultaneous attenuation and detector response correction in SPECT. IEEE Trans Nucl Sci 1988;35:778–83.
[2] Leahy R, Byrne C. Recent developments in iterative image reconstruction for PET and SPECT. IEEE Trans Med Imaging 2000;19:257–60.
[3] DePuey EG. Advances in SPECT camera software and hardware: Currently available and new on the horizon. J Nucl Cardiol 2012;19:551–81.
[4] Hudson HM, Larkin RS. Accelerated image reconstruction using ordered subsets of projection data. IEEE Trans Med Imaging 1994;13:601–9.
[5] Shepp LA, Vardi Y. Maximum Likelihood Reconstruction for Emission Tomography. IEEE Trans Med Imaging 1982;1:113–22.
[6] Bruyant PP. Analytic and Iterative Reconstruction Algorithms in SPECT. J Nucl Med 2002;43:1343–58.
[7] Green PJ. Bayesian reconstructions from emission tomography data using a modified EM algorithm. IEEE Trans Med Imaging 1990;9:84–93.
[8] Kangasmaa T, Sohlberg A, Kuikka JT. Reduction of Collimator Correction Artefacts with Bayesian Reconstruction in Spect. Int J Mol Imaging 2011;2011:1–6.
[9] Mustafovic S, Thielemans K. Additive and multiplicative versions of the maximum a posteriori algorithm with median root prior. Nuclear Science Symposium Conference Record, IEEE 2001.
[10] Aldridge MD, Waddington WW, Dickson JC, Prakash V, Ell PJ, Bomanji JB. Clinical evaluation of reducing acquisition time on single-photon emission computed tomography image quality using proprietary resolution recovery software. Nucl Med Commun 2013;34:1116–23.
[11] Sun XX, Tian YQ, Wang DY, He ZX. Shortened acquisition time or reduced-activity dose for gated myocardial perfusion SPECT with new reconstruction algorithm. Int J Cardiovasc Imaging 2013;29:1287–93.
[12] He B, Frey EC. Effects of shortened acquisition time on accuracy and precision of quantitative estimates of organ activity. Med Phys 2010;37:1807–15.
[13] Molina-Duran F, Dinter D, Schoenahl F, Schoenberg SO, Glatting G. Dependence of image quality on acquisition time for the PET/CT Biograph mCT. Z Med Phys 2014;24:73–9.
[14] Kangasmaa TS, Kuikka JT, Vanninen EJ, Mussalo HM, Laitinen TP, Sohlberg AO. Half-time myocardial perfusion SPECT imaging with attenuation and Monte Carlo-based scatter correction. Nucl Med Commun 2011;32:1040–5.
[15] Stansfield EC, Sheehy N, Zurakowski D, Vija AH, Fahey FH, Treves ST. Pediatric 99mTc-MDP Bone SPECT with Ordered Subset Expectation Maximization Iterative Reconstruction with Isotropic 3D Resolution Recovery. Radiology 2010;257:793–801.
[16] Zeintl J, Vija AH, Yahil A, Hornegger J, Kuwert T. Quantitative Accuracy of Clinical 99mTc SPECT/CT Using Ordered-Subset Expectation Maximization with 3-Dimensional Resolution Recovery, Attenuation, and Scatter Correction. J Nucl Med 2010;51:921–8.
[17] Vija AH, Hawman EG, Engdahl JC, editors. Analysis of a SPECT OSEM reconstruction method with 3D beam modeling and optional attenuation correction: phantom studies. Nuclear Science Symposium Conference Record IEEE 2003.
[18] Daube-Witherspoon M, Karp J, Casey M, DiFilippo F, Hines H, Muehllehner G, et al. Performance Measurements of Positron Emission Tomographs (PETs). National Electrical Manufacturers Association NEMA standards publication NU2-2012 2013.
[19] Kalra MK, Naz N, Rizzo SMR, Blake MA. Computed Tomography Radiation Dose Optimization: Scanning Protocols and Clinical Applications of Automatic Exposure Control. Curr Probl Diagn Radiol 2005;34:171–81.
[20] Knoll P, Kotalova D, Köchle G, Kuzelka I, Minear G, Mirzaei S, et al. Comparison of advanced iterative reconstruction methods for SPECT/CT. Z Med Phys 2012;22:58–69.
[21] Mulchrone KF, Choudhury KR. Fitting an ellipse to an arbitrary shape: implications for strain analysis. Journal of Structural Geology 2004;26:143–53.
[22] Razifar P, Sandstrom M, Schnieder H, Langstrom B, Maripuu E, Bengtsson E, et al. Noise correlation in PET, CT, SPECT and PET/CT data evaluated using autocorrelation function: a phantom study on data, reconstructed using FBP and OSEM. BMC Med Imaging 2005;5:5.
[23] Tong S, Alessio AM, Kinahan PE. Evaluation of noise properties in PSF-based PET image reconstruction. Nuclear Science Symposium Conference Record (NSS/MIC), IEEE; 2009.
[24] Vija AH. Introduction to xSPECT Technology. Siemens Medical Solutions White Paper 2013:1–27.
[25] Vija AH, Yahil A, Hawman EG. Preprocessing of SPECT projection data: benefits and pitfalls. Nuclear Science Symposium Conference Record, IEEE 2005.
[26] Takalo R, Hytti H, Ihalainen H, Sohlberg A. Adaptive Autoregressive Model for Reduction of Noise in SPECT. Comput Math Methods Med 2015;2015:9.
[27] Römer W, Reichel N, Vija HA, Nickel I, Hornegger J, Bautz W, et al. Isotropic Reconstruction of SPECT Data Using OSEM3D: Correlation with CT. Acad Radiol 2006;13:496–502.
[28] Li Y. Noise propagation for iterative penalized-likelihood image reconstruction based on Fisher information. Phys Med Biol 2011;56:1083–103.
[29] Barrett HH, Wilson DW, Tsui BMW. Noise properties of the EM algorithm: I. Theory. Phys Med Biol 1994;39:833–46.
[30] Wang W, Gindi G. Noise analysis of MAP - EM algorithms for emission tomography. Phys Med Biol 1997;42:2215–32.
[31] Fessler JA. Mean and variance of implicitly defined biased estimators (such as penalized maximum likelihood): applications to tomography. IEEE Trans Image Process 1996;5:493–506.
[32] Ritt P, Sanders J, Kuwert T. SPECT/CT technology. Clin Transl Imaging 2014;2:445–57.
[33] Kazantsev D, Arridge SR, Pedemonte S, Bousse A, Erlandsson K, Hutton BF, et al. An anatomically driven anisotropic diffusion filtering method for 3D SPECT reconstruction. Phys Med Biol 2012;57:3793–810.
[34] Comtat C, Kinahan PE, Fessler JA, Beyer T, Townsend DW, Defrise M, et al. Clinically feasible reconstruction of 3D whole-body PET/CT data using blurred anatomical labels. Phys Med Biol 2002;47:1–20.